

# Multiscale insights into classical geomechanics problems

Ning Guo<sup>\*,†</sup> and Jidong Zhao

*Department of Civil and Environmental Engineering, The Hong Kong University of Science and Technology, Clear Water Bay, Kowloon, Hong Kong*

## SUMMARY

We pay a revisit to some classical geomechanics problems using a novel computational multiscale modelling approach. The multiscale approach employs a hierarchical coupling of the finite element method (FEM) and the discrete element method. It solves a boundary value problem at the continuum scale by FEM and derives the material point response from the discrete element method simulation attached to each Gauss point of the FEM mesh. The multiscale modelling framework not only helps successfully bypass phenomenological constitutive assumptions as required in conventional modelling approaches but also facilitates effective cross-scale interpretation and understanding of soil behaviour. We examine the classical retaining wall and footing problems by this method and demonstrate that the simulating results can be well validated and verified by their analytical solutions. Furthermore, the study sheds novel multiscale insights into these classical problems and offers a new tool for geotechnical engineers to design and analyse geotechnical applications based directly upon particle-level information of soils. Copyright © 2015 John Wiley & Sons, Ltd.

Received 27 October 2014; Revised 19 May 2015; Accepted 2 June 2015

KEY WORDS: multiscale modelling; FEM/DEM; retaining wall; footing; strain localisation

## 1. INTRODUCTION

The design in geotechnical engineering had largely been empirically based until a series of theoretical advances was made by pioneers in soil mechanics in the early 20th century. They are best known today as lateral earth pressure theory, bearing capacity theory, consolidation theory, limit theorem and so on [1–6]. The complexity of real geotechnical problems, however, can frequently exceed the scope and capability of these over-simplified theories can handle. More advanced and robust methods have been badly needed to solve the increasingly complicated practical problems met in urban developments around the world. The 1960s marked an era of great changes for both soil mechanics and geotechnical design, when modern soil mechanics represented by the plasticity-based critical state constitutive models were developed and computer and numerical tools such as the finite element method (FEM) were made accessible to geotechnical engineers. The past half-century has indeed witnessed the flourishing of various computer-aided continuum constitutive modelling approaches in application to every aspect of geotechnical engineering.

Core to continuum modelling of a geotechnical problem is the assumed constitutive model to capture the essential material behaviour of soil under variable loading conditions. The fact that there have been hundreds (if not more) of different soil models in the literature partially explains how complex the soil behaviour can be and how difficult it is to characterise. It is common that one model may successfully capture some features of the soil response but fails miserably for many others. Take granular soils as an example. Numerous laboratory tests show that a granular

---

\*Correspondence to: Ning Guo, Department of Civil and Environmental Engineering, The Hong Kong University of Science and Technology, Clear Water Bay, Kowloon, Hong Kong.

†E-mail: ceguo@connect.ust.hk

soil may exhibit intriguing mechanical responses under shear, ranging from state and loading-path dependence, non-coaxiality [7, 8], anisotropy [9–11], liquefaction, cyclic mobility to critical state [12, 13]. Its behaviour becomes more complicated or even intractable when being considered in a context of practical engineering problems. A constitutive model, however well calibrated and verified by laboratory test data, may provide inadequate, inaccurate or totally wrong predictions for large-scale engineering-level boundary value problems (BVPs). Not only is this caused by the heterogeneous nature in soil properties and the complexity involved in the boundary conditions of an engineering problem but it may also be attributable to the extremely diversified loading paths and soil states that the material points at different locations of the physical domain may experience. Moreover, complicated phenomena such as strain localisation and liquefaction [14–20] may occur in a geotechnical problem. To capture all these perplexing features pose formidable challenges for continuum constitutive modellers. To gain better predictive capability, one has to develop models with many model parameters, which are frequently phenomenological in nature and difficult to calibrate. This apparently forfeits their ultimate goal to facilitate their easy use for practising geotechnical engineers.

The key factor attributable to the limitations for continuum theories has indeed been pinpointed by Terzaghi in 1920 [21], when he argued that his predecessor Coulomb had ‘purposely ignored the fact that sand consists of individual grains, and ... deal with the sand as if it were a homogeneous mass with certain mechanical properties. Coulomb’s idea proved very useful as a working hypothesis for the solution of one special problem of the earth-pressure theory, but it developed into an obstacle against further progress as soon as its hypothetical character came to be forgotten by Coulomb’s successors. The way out of the difficulty lies in dropping the old fundamental principles and starting again from the elementary fact that sand consists of individual grains’. The discrete nature in sand gives rise to an easily identifiable multiscale hierarchy when it is compared with a relevant engineering problem, as shown in Figure 1. Terzaghi has indeed envisioned a picture of cross-scale modelling for sand; however, the pathway to there was neither easy nor trivial. It was not until 60 years later when Cundall and Strack [22] developed their seminal tool of the discrete element method (DEM) before Terzaghi’s envisioned approach can be effectively executed. DEM has been widely used in the past 30 years for sand behaviour characterisation with considerable success. However, it can at best be used as a virtual laboratory testing tool for now and can quickly become inept to deal with practical engineering-scale problems because of constraints on allowable particle number and computational efficiency.

To circumvent the difficulties of both continuum and purely discrete-based approaches mentioned earlier, we employ in this study a computational multiscale approach to treat geotechnical BVPs. This approach is based on a hierarchical coupling of FEM and DEM to capture the multiscale hierarchy shown in Figure 1. It uses FEM to simulate the physical domain of a BVP and hence is able to retain its computational efficiency while avoiding using phenomenological constitutive models by extracting material response from separate DEM simulation at each Gauss point of the FEM mesh where the discrete nature of sand at the microscale is fully respected. The scenario of

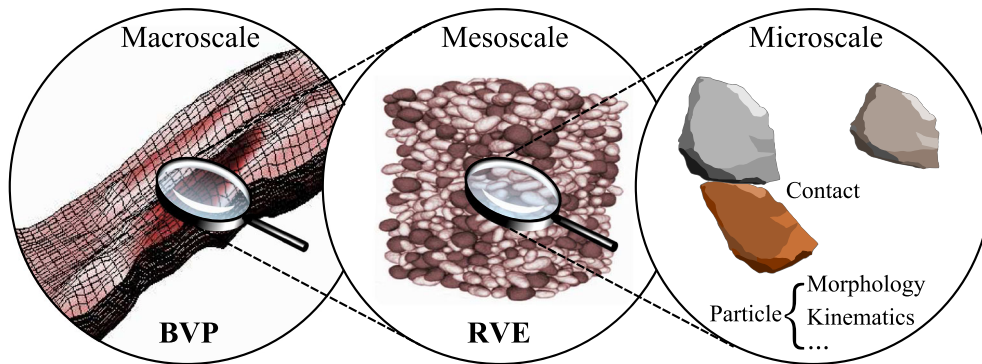


Figure 1. Schematic illustration of the scale separation in sand and its hierarchical multiscale modelling.

cross-scale modelling as envisaged by Terzaghi can now be realised with ease. The multiscale approach employed in this study was recently developed by the authors [23–26], which is also inline with some recent studies [27–31]. In this study, we further introduce rolling resistance to the DEM model to better account for the effect of particle shape on the strength and deformation of sand/gravel. Two classical geotechnical problems were selected for simulation by the multiscale modelling approach, namely, the retaining wall and the footing.

## 2. METHODOLOGY AND FORMULATION

The multiscale approach employs the FEM to discretise the macroscopic continuum domain and solve it as a BVP. Iterative Newton–Raphson scheme is employed to tackle non-linear sand response. The material response at each Gauss point is derived based on DEM simulation on a representative volume element (RVE) packing of particles with suitable grain size distribution, contact and friction properties and initial states. Because each RVE receives the deformation at the specific Gauss point as local boundary condition and keeps its memory of immediate past state during each incremental loading step of the FEM solution, it can naturally capture the highly non-linear history-dependent behaviour of sand. The formulations of the multiscale framework are briefly presented in the following. Although the current paper deals with two-dimensional (2D) simulations, most of the following formulations are applicable to general three-dimensional cases unless explicitly stated otherwise.

### 2.1. FEM solver

For the quasi-static problem in the absence of gravity, the governing equilibrium equation writes

$$\nabla \cdot \boldsymbol{\sigma} = \mathbf{0}, \quad (1)$$

where  $\boldsymbol{\sigma}$  is the stress tensor. Its variational form can be obtained by applying the principle of virtual work

$$\int_{\Omega} \delta \boldsymbol{\varepsilon}^T \boldsymbol{\sigma} \, d\Omega = W^{\text{ext}}, \quad (2)$$

where  $\Omega$  denotes the problem domain,  $W^{\text{ext}}$  ( $= \mathbf{f}^{\text{ext}} \delta \mathbf{u}$ ) is the virtual work performed by the external force  $\mathbf{f}^{\text{ext}}$ ,  $\delta \mathbf{u}$  is a variation of the primary unknown displacement  $\mathbf{u}$ , and  $\delta \boldsymbol{\varepsilon}$  ( $= \mathbf{B} \delta \mathbf{u}$ ) is the variational strain where  $\mathbf{B}$  is the displacement–strain matrix after FEM discretisation. Equation 2 can then be rewritten as follows by eliminating  $\delta \mathbf{u}$

$$\int_{\Omega} \mathbf{B}^T \boldsymbol{\sigma} \, d\Omega = \mathbf{f}^{\text{ext}} \quad (3)$$

based on which the stiffness matrix  $\mathbf{K}$  can be readily obtained using  $\boldsymbol{\varepsilon} = \mathbf{B}\mathbf{u}$  and  $\boldsymbol{\sigma} = \mathbf{D}\boldsymbol{\varepsilon}$ :

$$\mathbf{K} = \int_{\Omega} \mathbf{B}^T \mathbf{D} \mathbf{B} \, d\Omega, \quad (4)$$

where  $\mathbf{D}$  is the material modulus for linear problems. The final discrete equation system can be formulated as below

$$\mathbf{K} \mathbf{u} = \mathbf{f}^{\text{ext}}. \quad (5)$$

For a general non-linear problem,  $\mathbf{D}$  is the tangent operator used to find trial solutions for FEM. The Newton–Raphson iterative scheme is employed to find the converged solution to Equation 5. In a displacement-driven FEM, the deformation (displacement gradient)  $\nabla \mathbf{u}$  at each Gauss point of the FEM mesh can be interpolated from the nodal displacement and is then applied as the local boundary condition for the corresponding RVE packing to resolve for a DEM solution. Based on the

RVE solution, the stress tensor  $\boldsymbol{\sigma}$  and the tangent operator  $\mathbf{D}$  are then homogenised and updated. The specific formulations for  $\boldsymbol{\sigma}$  and  $\mathbf{D}$  will be provided in Section 2.3. A converged solution is sought by evaluating the residual force  $\mathbf{R}$  in comparison with a prescribed tolerance

$$\mathbf{R} = \int_{\Omega} \mathbf{B}^T \boldsymbol{\sigma} \, d\Omega - \mathbf{f}^{\text{ext}}. \quad (6)$$

More detailed description of the solution procedure can be found in [23–26].

## 2.2. DEM solver

We use cylindrical particles (rods) in the RVE packing to approximately simulate the plane-strain behaviour of sand.<sup>‡</sup> To fairly reproduce the strength of sand, a simple DEM model with rolling resistance is used to describe the interparticle contact. The contact normal force  $\mathbf{f}_n^c$  and the tangential frictional force  $\mathbf{f}_t^c$  are assumed to be governed by a linear force–displacement law:

$$\mathbf{f}_n^c = -k_n \delta \mathbf{n}^c, \quad (7)$$

$$\mathbf{f}_t^c = \begin{cases} -k_t \mathbf{u}_t^c, & \text{if } |\mathbf{f}_t^c| \leq |\mathbf{f}_n^c| \tan \varphi \\ |\mathbf{f}_n^c| \tan \varphi \mathbf{t}^c, & \text{otherwise} \end{cases} \quad (8)$$

where  $\delta$  is the overlap of the two contacting particles,  $\mathbf{n}^c$  is the unit outward normal of the contact,  $\mathbf{u}_t^c$  is the accumulated relative tangential displacement at the contact,  $\mathbf{t}^c (= -\mathbf{u}_t^c/|\mathbf{u}_t^c|)$  is the unit vector along the tangential direction of the contact and  $\varphi$  is the interparticle friction angle (Figure 2). The contact normal and the tangential stiffnesses are determined by the Young’s modulus  $E_c$  and the Poisson’s ratio  $\nu_c$  of the particles:

$$\begin{cases} k_n = E_c r^*, \\ k_t = \nu_c k_n, \end{cases} \quad (9)$$

where  $r^* = 2r_1 r_2 / (r_1 + r_2)$  is the common radius of the two contacting particles with radii  $r_1$  and  $r_2$ , respectively. To approximate quasi-static condition and dissipate kinetic energy, an extra local non-viscous damping force  $\mathbf{f}^{\text{damp}}$  is added opposite to the particle velocity direction and is made proportional to the magnitude of the unbalanced force  $\mathbf{f}^{\text{unbal}}$  of the particle with a damping ratio  $\alpha$

$$\mathbf{f}^{\text{damp}} = -\alpha |\mathbf{f}^{\text{unbal}}| \mathbf{v}/|\mathbf{v}|. \quad (10)$$

The resultant contact force (and only tangential force for circular particles) will exert a moment on the particle, which serves as the only driver of particle rolling in the free-rotation case. It is well recognised that DEM simulations based on free-rotation assumption and circular particles greatly underestimate the strength of sand as compared with laboratory tests [32]. Because sand grains are commonly angular with rough surfaces, surface (rather than point) contacts and interlocking may prevail in the interparticle contacts. These factors may sum up to generate an anti-rotation effect for the particles, which will be described by a rolling resistance model in this study. In this rolling resistance model, the contact moment  $\mathbf{M}_r$  is written in a similar way to the tangential force [33, 34]

$$\mathbf{M}_r = \begin{cases} -k_r \boldsymbol{\theta}_r^c, & \text{if } |\mathbf{M}_r| \leq |\mathbf{f}_n^c| r_{\min} \eta \\ -|\mathbf{f}_n^c| r_{\min} \eta \boldsymbol{\theta}_r^c / |\boldsymbol{\theta}_r^c|, & \text{otherwise} \end{cases} \quad (11)$$

where  $\boldsymbol{\theta}_r^c$  is the accumulated relative rotation at the contact,  $\eta$  is the rolling resistance coefficient in analogy to the role of frictional coefficient, which imposes a threshold for the contact moment

<sup>‡</sup>It should be noted 2D DEM test is only a qualitative approximation rather than an equivalence of plane-strain test on real sand.

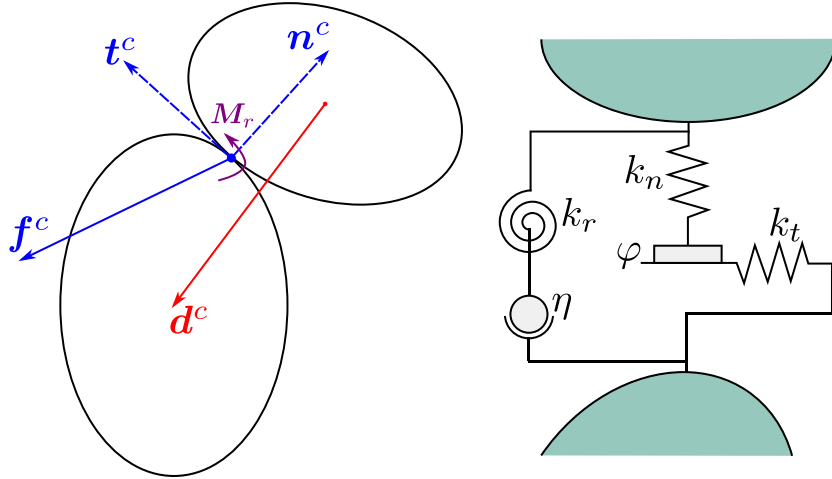


Figure 2. Illustration of the contact model in discrete element method accounting for rolling resistance.

beyond which particle rotation may be mobilised, and  $r_{\min}$  is the minimum radius between  $r_1$  and  $r_2$ . The rolling stiffness  $k_r$  (Figure 2) is linked to the tangential stiffness  $k_t$  and another parameter  $\beta_c$  through

$$k_r = \beta_c k_t r_1 r_2. \quad (12)$$

Details on the implementation of the DEM model are documented in the YADE manual [35].

### 2.3. RVE homogenisation

The RVE packing chosen in the study contains 400 polydisperse circular (cylindrical) particles with radii ranging from 3 to 7 mm and a particle density of  $2650 \text{ kg/m}^3$ . A thickness of 0.1 m is assumed for the packing to maintain the stress measurement in pressure unit (i.e. force over area). Periodic boundary conditions are applied to both dimensions of the packing. The homogenised stress tensor of the packing is obtained from the Love formula

$$\boldsymbol{\sigma} = \frac{1}{V} \sum_{N_c} \mathbf{d}^c \otimes \mathbf{f}^c, \quad (13)$$

where  $V$  is the volume of the RVE packing,  $N_c$  is the number of contacts within the packing,  $\mathbf{d}^c$  is the branch vector connecting the centres of the two contacting particles (Figure 2) and  $\mathbf{f}^c$  is the contact force. Two common stress measurements – the mean effective stress  $p$  and the deviatoric stress  $q$  – can be calculated accordingly (in 2D)

$$\begin{cases} p = \frac{1}{2} \text{tr} \boldsymbol{\sigma}, \\ q = \sqrt{\frac{1}{2} \mathbf{s} : \mathbf{s}}, \end{cases} \quad (14)$$

where  $\mathbf{s}$  is the deviatoric stress tensor. The strain field is interpreted from the FEM solution, that is, the gradient of the displacement  $\nabla \mathbf{u}$

$$\boldsymbol{\varepsilon} = -\frac{\nabla \mathbf{u} + \nabla^T \mathbf{u}}{2}, \quad (15)$$

where compression is taken as positive so a minus sign is present. The volumetric strain  $\varepsilon_v$  and the deviatoric strain  $\varepsilon_q$  can then be calculated (in 2D)

$$\begin{cases} \varepsilon_v = \text{tr } \boldsymbol{\varepsilon}, \\ \varepsilon_q = \sqrt{2 \boldsymbol{\varepsilon} : \boldsymbol{\varepsilon}}, \end{cases} \quad (16)$$

where  $\boldsymbol{\varepsilon}$  is the deviatoric strain tensor. Note that the displacement gradient  $\nabla \mathbf{u}$  will be applied as local boundary conditions for the DEM simulations to deform the RVE packing. In addition to strain, it indeed includes an overall rotation  $\boldsymbol{\omega} = (\nabla^T \mathbf{u} - \nabla \mathbf{u})/2$  as well to accommodate large deformation in strain localisation problems. The tangent operator needed to assemble the FEM stiffness matrix is given based on the uniform strain assumption [36–38]

$$\mathbb{D} = \frac{1}{V} \sum_{N_c} (k_n \mathbf{n}^c \otimes \mathbf{d}^c \otimes \mathbf{n}^c \otimes \mathbf{d}^c + k_t \mathbf{t}^c \otimes \mathbf{d}^c \otimes \mathbf{t}^c \otimes \mathbf{d}^c). \quad (17)$$

The rank-four tensor  $\mathbb{D}$  can be written in the matrix form  $\mathbf{D}$  (e.g. via Voigt notation) to be used in Equation 4. Note also that the interparticle rolling stiffness has no effect in calculating the tangent operator and the stiffness matrix, as only Cauchy stress is used (Equation 13). If the couple stress is considered, for example because of the interparticle contact moments [39], the rolling stiffness needs to be properly incorporated into Equation 17.

### 3. RETAINING WALL

The model set-up of the retaining wall problem follows similarly that presented in [15, 40]. A domain of 0.4 m in length and 0.2 m in depth is modelled. A rigid retaining wall with the height of  $h = 0.17$  m is positioned at the right side of the backfill soil. A uniformly distributed surcharge  $q_s = 20$  kPa is applied on the top surface of the backfill soil. The surface of the retaining wall is assumed rough (no relative vertical displacement between wall and soil) under three wall movement modes (translation and rotation about the top and the bottom), and another special case with smooth wall (no shear stress at the interface between wall and soil) is considered for the translation mode. The soil domain is discretised by a FEM mesh of  $40 \times 20$  eight-node quadrilateral elements with reduced integration (four Gauss points) as shown in Figure 3(a). The quadratic element adopted here is found helpful to eliminate the pathological dependence on mesh density of FEM solutions.<sup>§</sup> The reduced integration can efficiently save the computational cost and meanwhile provide accurate results compared with the full integration [26]. With all Gauss points counted, the simulation involves 3200 RVE packings containing a total of 1.28 million particles for each iteration. With parallelisation on an HP SL230 Gen8 (Hewlett-Packard, Palo Alto, California, USA) server ( $2 \times 8$ -core 2.6 GHz CPU), each test in this section costs 10 to 15 h. Three different modes of wall movement are considered under both passive and active failure conditions, which are illustrated in Figure 3(b). All RVE packings are first anisotropically consolidated to a state with a vertical stress (in  $x_1$  direction) of  $\sigma_{v0} = 20$  kPa and a horizontal stress (in  $x_0$  direction) of  $\sigma_{h0} = 10$  kPa, that is, the at-rest lateral earth pressure coefficient assumed  $K_0 = \sigma_{h0}/\sigma_{v0} = 0.5$  and initial void ratio of  $e_0 = 0.182$ . The RVEs are then assigned to their respective Gauss points of the FEM mesh. This leads to an initially uniform domain. Gravity is neglected in the simulation.

#### 3.1. DEM model and RVE effective friction angle

The microscopic parameters in the DEM model for the retaining wall problem are summarised in Table I. Similar parameters have been used in previous studies [41]. For practical interpretation in engineering applications, it is usually more convenient to use a macroscopic measurement such as the effective friction angle  $\varphi'$  as frequently used in a Mohr–Coulomb criterion. Due to the non-linear

<sup>§</sup>The insensitivity of the result to the mesh density using quadratic elements is observed from additional biaxial compression tests, which are not presented here to avoid distraction of focus.

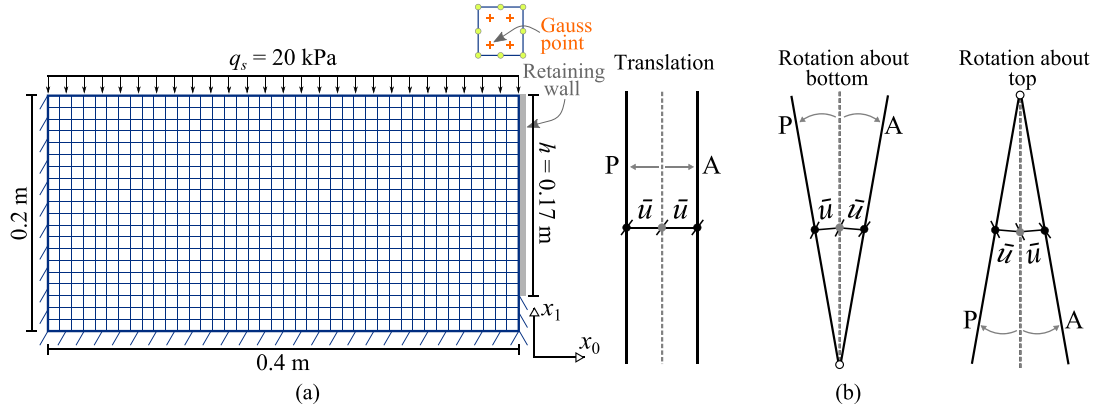


Figure 3. Model set-up on the simulation of retaining wall: (a) mesh and boundary conditions and (b) three modes of wall movement to trigger either passive or active failure condition in the backfill soil.

Table I. Parameters for the DEM model used in the retaining wall problem.

$E_c$ (MPa)	$\nu_c$	$\beta_c$	$\varphi$ ( $^\circ$ )	$\eta$	$\alpha$
300	0.3	1.0	33	0.3	0.1

DEM, discrete element method.

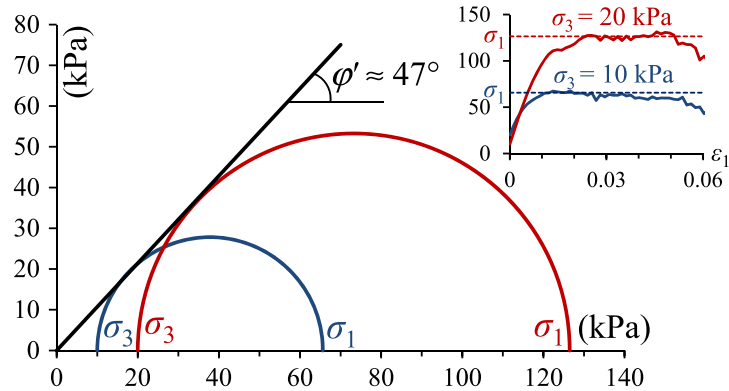


Figure 4. Estimation of the macroscopic effective friction angle of the representative volume element for the retaining wall problem.

nature in the material response,  $\varphi'$  is not a constant under shearing but will undergo steady changes related closely to the softening or hardening processes depending on the initial condition and the loading path.

To estimate the effective friction angle  $\varphi'$ , drained biaxial compression tests were performed on the RVE packing under two different confining pressure levels,  $\sigma_3 = 10$  and 20 kPa, respectively. The peak stress state (failure) points were extracted from the two tests to plot their corresponding Mohr's circles as shown in Figure 4. The effective friction angle is then approximately estimated from the envelope of the two circles as  $\varphi' \approx 47^\circ$  (assume zero cohesion). The value is relatively large and may correspond to some gravel materials or very dense sands [42].

### 3.2. Lateral earth pressure coefficient

The evolution of the lateral earth pressure coefficient, defined as the lateral earth pressure  $\sigma_h$  exerted on the wall surface normalised by the vertical stress ( $\sigma_v = q_s = 20$  kPa), against the average wall displacement  $\bar{u}$  (equivalent to the displacement at the centre of the wall; Figure 3(b)) normalised by

the height of the wall is plotted in Figure 5. The analytical predictions by the Rankine's theory [1] are comparatively presented, where the passive and the active earth pressure coefficients, denoted as  $K_p$  and  $K_a$  respectively, are given as follows:

$$\begin{cases} K_p = \tan^2 \left( \frac{\pi}{4} + \frac{\varphi'}{2} \right) \\ K_a = \tan^2 \left( \frac{\pi}{4} - \frac{\varphi'}{2} \right) \end{cases} \quad (18)$$

where  $\varphi'$  is the effective friction angle determined in Section 3.1.

As seen from Figure 5(a), when the wall moves towards the soil tending to create a passive failure condition, the lateral earth pressure is progressively mobilised towards a peak value (regarded as the passive lateral earth pressure here) where the corresponding normalised displacement of the wall  $\bar{u}/h$  ranges from 0.03 to 0.06 for the three modes of wall movement. It is noted the deformation level to reach the peak lateral earth pressure is larger than that presented in [40] (Figures 5(a) and 13(a) therein) because of a smaller stiffness adopted for the material here. In their discrete model [40], the contact modulus  $E_c$  was set to 30 GPa, while in the current study, the value adopts a much smaller value of 300 MPa to accelerate the DEM computation with a larger time step. The post peak response shows a pressure drop in all cases. Among them, the translation mode with rough wall surface yields the largest passive lateral earth pressure coefficient, which is about 1.8 times larger than the corresponding case with a smooth wall. The rotation-about-bottom mode with rough wall gives a passive lateral earth pressure coefficient in between the above two modes, and its value almost coincides with the analytical prediction based on the Rankine's theory  $K_p = 6.44$ . The rotation-about-top mode gives the smallest passive lateral earth pressure coefficient of all. A general observation of the passive modes for the four cases indicates that a larger wall movement is needed to mobilise the higher peak pressure.

The soil responses under the active failure mode differ substantially from the passive cases. As shown in Figure 5(b), the lateral earth pressures for all cases decrease almost instantly when the wall movement is applied and reach a minimum (considered as the active lateral earth pressure) before increasing again. Among the four, the translation mode with a rough wall yields the smallest active lateral earth pressure coefficient at about 0.15, and the value is only slightly higher in the corresponding smooth case than in the rough case. This is in strong contrast with the vast difference between the two cases in the passive condition. The analytical prediction based on the Rankine's theory  $K_a = 0.16$  is between the two translation mode results but is rather close to that of the rough translational wall case. Both rotation wall cases lead to bigger active lateral earth pressure coefficients than the translation cases, and the result of the rotation-about-top mode gives the largest

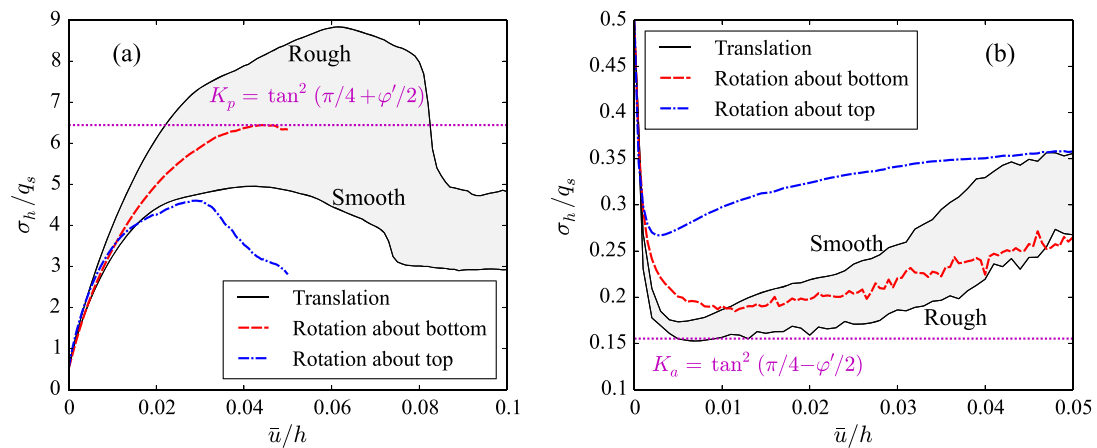


Figure 5. Evolution of lateral earth pressure coefficient with the wall movement under (a) the passive and (b) the active failure conditions.

of all. These observations are indeed consistent with the FEM simulations reported in [15, 40] based on a micropolar hypoplastic sand model, where the model parameters had been calibrated against the experimental data on Karlsruhe sand. The different observations of lateral earth pressure evolution in different failure modes with different wall movements signify different progressive failure patterns and different underlying micromechanical mechanisms in the backfill soil, which are examined in detail in the sequel.

3.3. Shear-zone pattern

3.3.1. Passive failure. The apparent post-peak drop of lateral pressure in Figure 5(a) in each case is accompanied with the occurrence of well-developed shear band(s) in the backfill soil. Towards the end of the loading, stabilised shear zones are observed. Figure 6 presents the shear-zone patterns, in terms of the accumulated shear strain  $\varepsilon_q$  and the void ratio  $e$ , at the end of wall movement in the passive condition. For the case of translation mode with a rough wall (Figure 6(a)), the shear zones

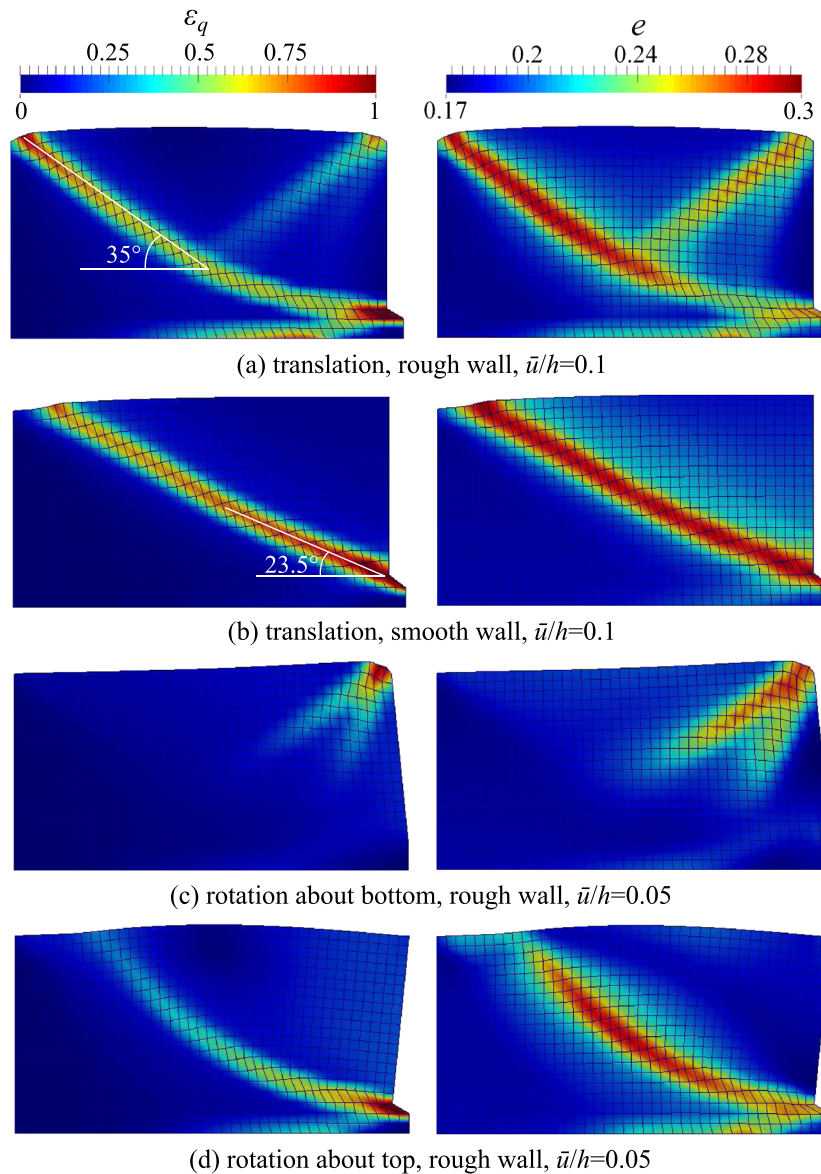


Figure 6. Contours of accumulated shear strain (left panel) and void ratio (right panel) for different failure modes under the passive condition.

depict two slip lines. The primary slip line consists of a spiral curve emanating from the bottom of the wall and a straight line developing towards the top surface of the backfill soil. The secondary slip line initiates from the top of the wall extending towards the primary one at the connecting point of the spiral segment and the straight line segment where it is intersected and cannot extend further down. Shear strains and volume dilation are less intense in the second shear zone than in the first. Notably, the second slip line essentially splits the soil body above the first one into two largely rigid triangle wedges with apparently different kinematic characteristics. The wedge bounded by the two lines and the wall features a roughly horizontal displacement, while the one above the two slip lines moves mainly upwards.

Interestingly, the use of a smooth wall for the same translation mode leads to a single localised shear zone only, which is a roughly straight line (Figure 6(b)). The soil wedge above the shear zone moves up-leftwards during the loading. Apparently, the constraint of wall on the vertical movement of adjacent soil results in the different observations in the rough and the smooth wall cases. Rankine's passive lateral earth pressure theory gives a theoretical angle of the passive failure slip line with respect to the horizontal plane of  $\pi/4 - \phi'/2 \approx 21.5^\circ$ . By comparing with two straight lines in the rough and the smooth wall cases, it is found the smooth wall case yields a very close value, which is measured as  $23.5^\circ$ , while the rough wall case gives a much higher inclination angle of the slip line, which is about  $35^\circ$ . The boundary condition (the rough wall assumption) and the limited domain width could possibly attribute to this.

The rotation-about-bottom mode leads to two relatively short shear zones radiating from the top of the wall, with the higher one resembling the secondary shear line in the translation mode with a rough wall (Figure 6(c)). For the case of rotation about top (Figure 6(d)), the slip line is shown to be a spiral curve developing from the bottom of the wall towards the top surface of the backfill soil.

It is interesting to compare the current multiscale model predictions of the shear-zone patterns under the passive failure with those experimental observations on an initially dense backfill soil using X-ray and digital image correlation techniques reported in [40] (Figures 1 and 3 therein). In their experiments, the translational mode with a rough wall shows a similar double-shear-zone pattern – one distinct curvilinear shear zone starting from the heel of the wall to the free surface of the backfill soil accompanied by a weak secondary shear zone propagating from the wall top. Similarly, they observed a single curved shear zone developed from the heel of the wall to the soil surface for the rotation-about-top mode. The major difference between the current study and the experimental result in [40] lies in the rotation-about-bottom mode. Instead of two radially penetrating shear zones starting from the top of the wall as observed here, multiple parallel curved shear zones were observed near the top of the wall in [40]. The difference may be caused by the different material properties as the modelled soil here has a softer response than that used in the experiment (Figure 5). It could also be attributable to the boundary condition because the soil–wall interaction is much simplified in the present study.

In addition to the contours of shear strain and void ratio, the distribution of average particle rotation also serves as a good indicator of the shear zone in strain localisation problems [26]. Both experimental [43] and DEM studies [44] show that pronounced particle rotations take place inside localised shear strain regions. By virtue of the hierarchical multiscale method, the average particle rotation can be quantified for any material point in the continuum field from its underlying RVE simulation. Here, the average particle rotation  $\bar{\theta}$  over an RVE packing is defined as

$$\bar{\theta} = \frac{1}{N_p} \sum_{N_p} \theta^p, \quad (19)$$

where  $\theta^p$  is the accumulated rotation of an individual particle where anti-clockwise rotation is treated as positive. The contours of  $\bar{\theta}$  for the passive failure cases are shown in Figure 7. It is not surprising that the concentrated bands showing large particle rotations coincide well with those exhibiting large shear strains and dilation. For the translation failure mode with a rough wall (Figure 7(a)), the material points inside the primary shear zone experience anti-clockwise rotations at large, while those inside the secondary shear zone undergo clockwise rotations. For the translation failure mode using a smooth wall (Figure 7(b)) and the rotation-about-top failure mode

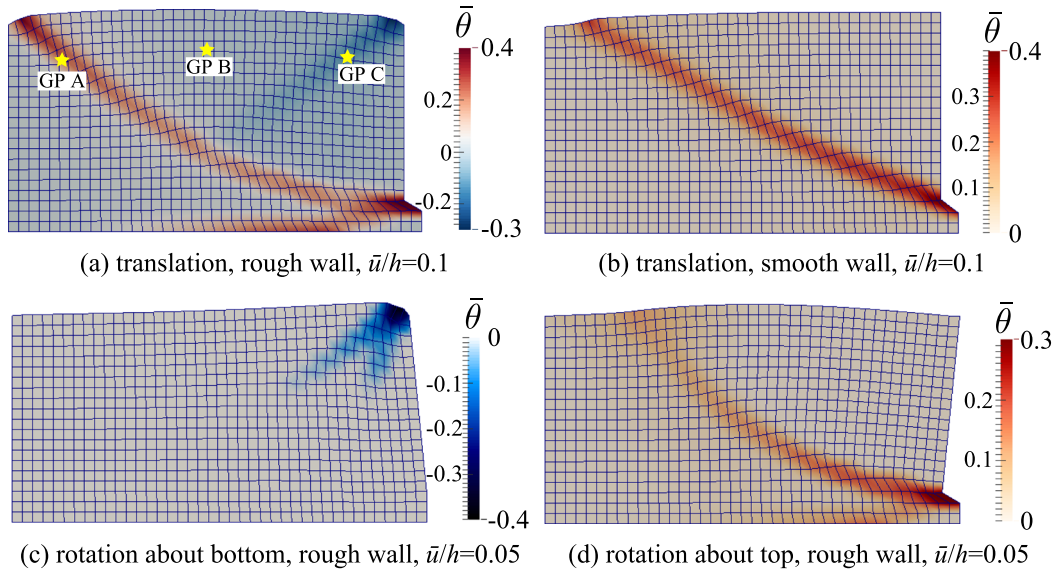


Figure 7. Contours of accumulated average particle rotation for different failure modes under the passive condition.

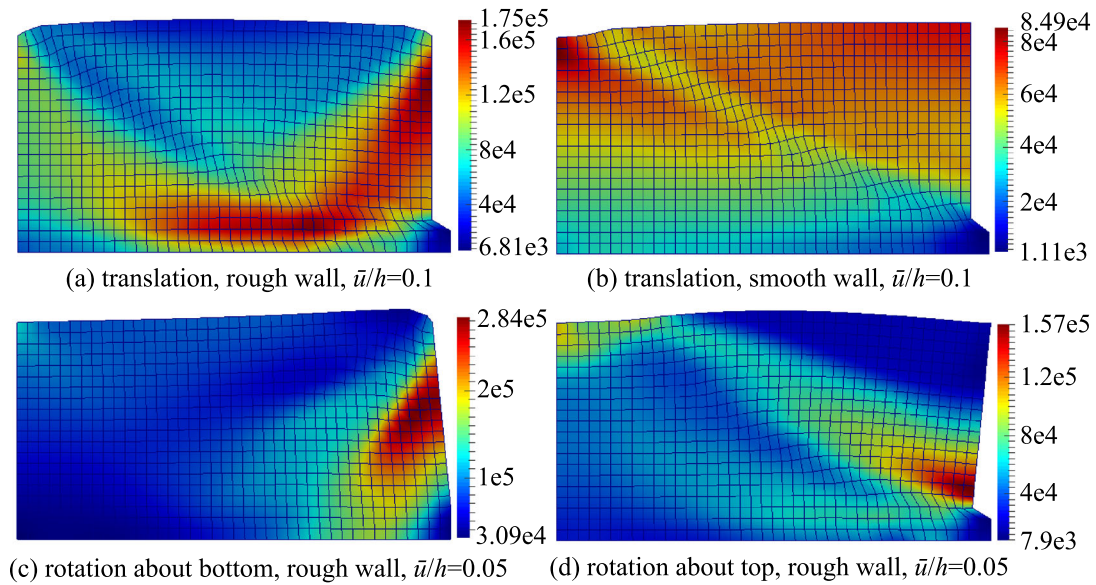


Figure 8. Contours of the stress norm  $\sqrt{\sigma : \sigma}$  for different failure modes under the passive condition.

(Figure 7(d)), large anti-clockwise particle rotations are observed within their respective shear zones. For the rotation-about-bottom failure mode (Figure 7(c)), clockwise particle rotation is dominant in the radiating shear zone. It is generally observed that when a shear slip line is initiated from the lower-right to the upper-left corner of the soil, anti-clockwise particle rotation dominates, and clockwise rotations prevail when a shear zone develops from the upper right to the lower left.

The stress distribution are also examined in Figure 8, where the stress measure employs the stress norm defined by  $\sqrt{\sigma : \sigma}$ . Generally, the stress intensities within the shear-localised zones are not necessarily the maximum because of stress softening, which implies that the stress contour is not a good indicator for strain localisation [26]. Under the translation mode with a rough wall (Figure 8(a)), the stress is mainly concentrated inside the triangle wedge behind the wall, while the wedge above the two slip lines has a minimum stress concentration. For the smooth wall

(Figure 8(b)), the stress field is relatively homogeneous in the region above the toe of the wall. Only the shear zone shows a slightly smaller stress norm because of shear softening. Because of the same reason, in the two rotation modes, a translation of the stress concentration zone during the loading procedure is observed. In the rotation-about-bottom mode (Figure 8(c)), the stress concentration moves downwards with a successive development of the shear-localised regions, leading the final stress concentration zone beneath the strain-localised zone. In contrast, the stress-concentrated zone moves upwards in the rotation-about-top mode (Figure 8(d)) and stays above the shear-localised zone at the final state.

3.3.2. *Active failure.* Figure 9 presents the shear-zone patterns for  $\varepsilon_q$  and  $e$  at the wall movement of  $\bar{u}/h = 0.05$  under the active failure condition. For the two translation modes with either a rough

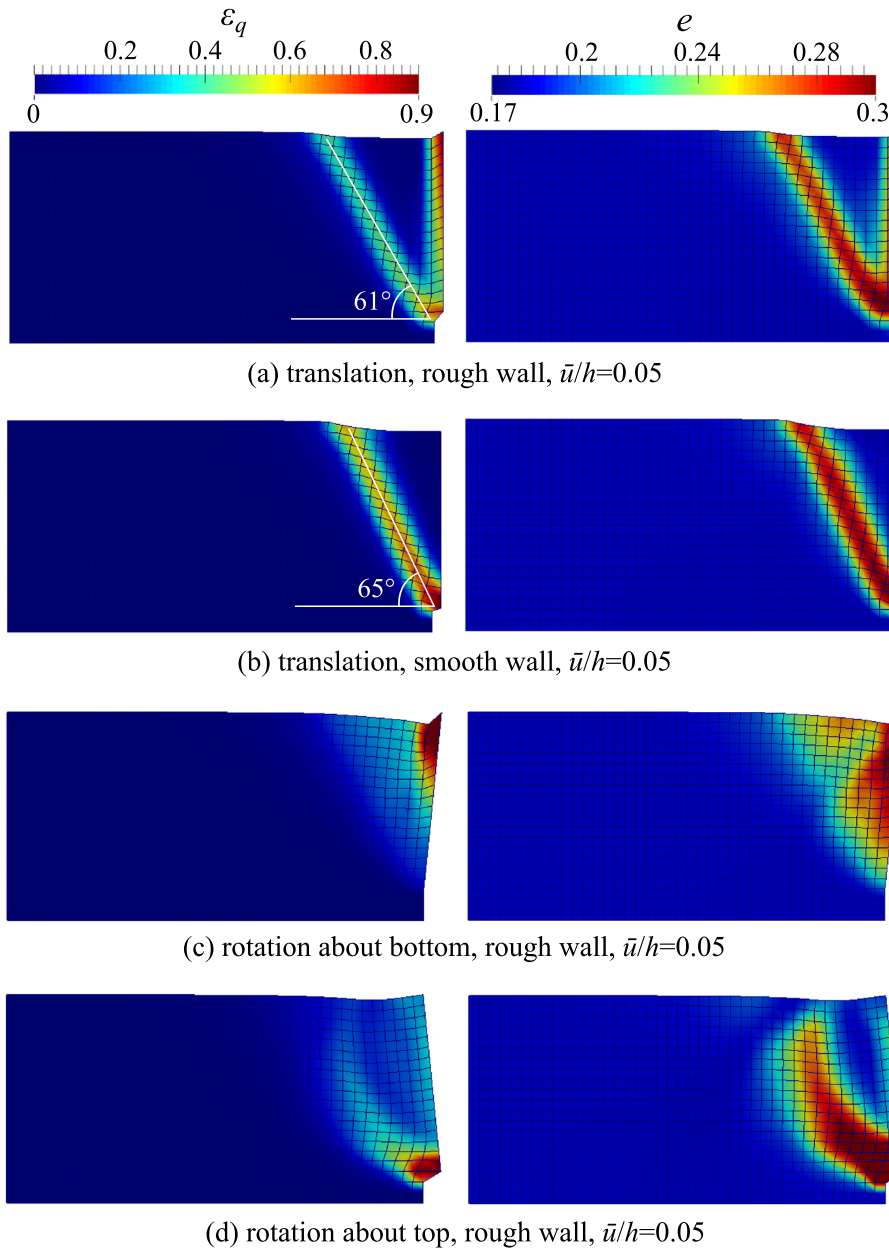


Figure 9. Contours of accumulated shear strain (left panel) and void ratio (right panel) for different failure modes under the active condition.

or a smooth wall (Figure 9(a) and (b)), a similar straight line of shear zone develops in the soil in both cases, and the wall–soil interface in the rough case appears to develop certain shear strain concentration too. The angle of the slip line with respect to the horizontal is  $61^\circ$  for the rough wall case and  $65^\circ$  for the smooth wall case. Both are close to the theoretical value calculated by the Rankine’s active lateral earth pressure theory:  $\pi/4 + \varphi'/2 \approx 68.5^\circ$ . For the rotation-about-bottom mode, multiple small failure zones form a relatively large triangular wedge behind the wall, which can be better identified from the contour of void ratio (Figure 9(c)). When the rotation is about the top of the wall, the shear zone depicts a thick spiral curve developing from the bottom of the wall towards the top surface of the backfill soil (Figure 9(d)). The curvature of the spiral curve is also much larger than in the corresponding passive condition case.

Again, the distributions of the average particle rotation  $\theta$  shown in Figure 10 are in good agreement with the contours of the shear strain and void ratio. Sand particles within the shear zones generally undergo large clockwise rotations (negative  $\theta$ ), but regions close to the rough wall surfaces (Figures 9(a),(c)&(d)) show relatively large anti-clockwise particle rotations because of the strong boundary constraint.

### 3.4. Local analyses

Featuring a major advantage, the current hierarchical multiscale approach enables us to offer cross-scale analyses for a complex BVP. The key macroscopic behaviours at important regions or positions of the macrodomain can be better understood and interpreted by their micromechanical origins extracted from the local RVE simulations. As a demonstration, here we choose several Gauss points for the cases of a rough wall under both passive and active translation modes to examine their local responses and microstructural changes. The selected Gauss points are marked in Figures 7(a) and 10(a) for the passive and active modes, respectively. They are initially located at the same height of the treated domain.

The evolutions of the stress ratio and the fabric anisotropy at the three Gauss points for the passive failure condition are plotted in Figure 11(a) against the wall displacement, where the fabric anisotropy is defined based on the contact normal distribution inside a local RVE packing [45, 46] (in 2D)

$$\begin{cases} \boldsymbol{\phi} = \frac{1}{N_c} \sum_{N_c} \mathbf{n}^c \otimes \mathbf{n}^c, \\ \mathbf{F}_c = 4 \times \text{dev } \boldsymbol{\phi}, \\ F_c = \sqrt{\frac{1}{2} \mathbf{F}_c : \mathbf{F}_c}, \end{cases} \quad (20)$$

where  $\boldsymbol{\phi}$  is the fabric tensor and  $\mathbf{F}_c$  is the deviatoric fabric tensor. A multiplier of 4 is present in calculating  $\mathbf{F}_c$  to ensure the integration of the distribution function  $E(\Theta)$  equal to 1, that is,  $\int_{\Theta} E(\Theta) d\Theta = 1$ , where  $E(\Theta) = [1 + \mathbf{F}_c : (\mathbf{n}^c \otimes \mathbf{n}^c)] / (2\pi)$ . The scalar  $F_c$  is used to measure the anisotropic intensity of the microstructure of the RVE packing. Figure 11(a) indicates the responses of the three Gauss points, in terms of both stress ratio  $q/p$  and fabric anisotropy  $F_c$ , are rather close, as summarised in the following stages. For the stress ratio  $q/p$ , (a) it first experiences a quick decrease at the beginning of the wall movement because of the flip of the major principal stress direction from the vertical axis at rest to the horizontal one under the passive failure; (b)  $q/p$  regains its strength and is then further mobilised to increase steadily until reaching a peak; and (c) after peak, an obvious softening in  $q/p$  is observed. The peak value of  $q/p$  for both GP A and GP C (inside the two shear zones) is about 0.7, which is consistent with that obtained from the element test in Figure 4. The wall displacement to reach the peak value for the two points ( $\bar{u}/h \approx 0.06$ ) is also consistent with that corresponding to the peak lateral earth pressure (rough wall, translation mode) in Figure 5(a). For GP B (outside the major shear zones), the peak  $q/p$  ( $\approx 0.63$ ) is slightly smaller as it undergoes a relatively small deformation; hence, its strength is not fully mobilised. The fabric anisotropy  $F_c$  increases monotonically to a peak value, at a slower pace than that of  $q/p$ , and then depicts a softening response coinciding with the softening stage of  $q/p$ . Figure 11(b) presents the

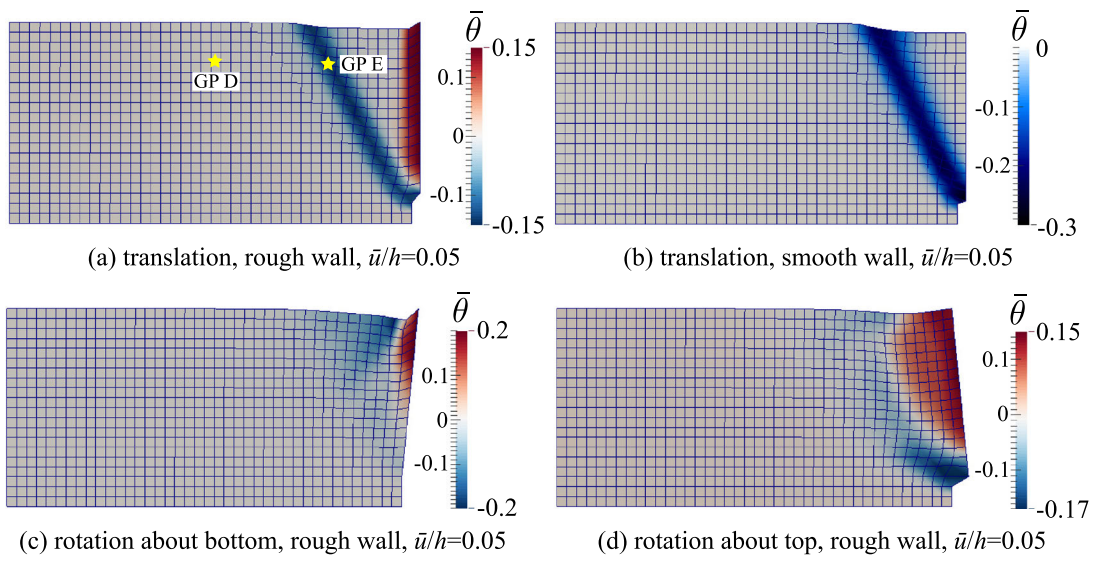


Figure 10. Contours of accumulated average particle rotation for different failure modes under the active condition.

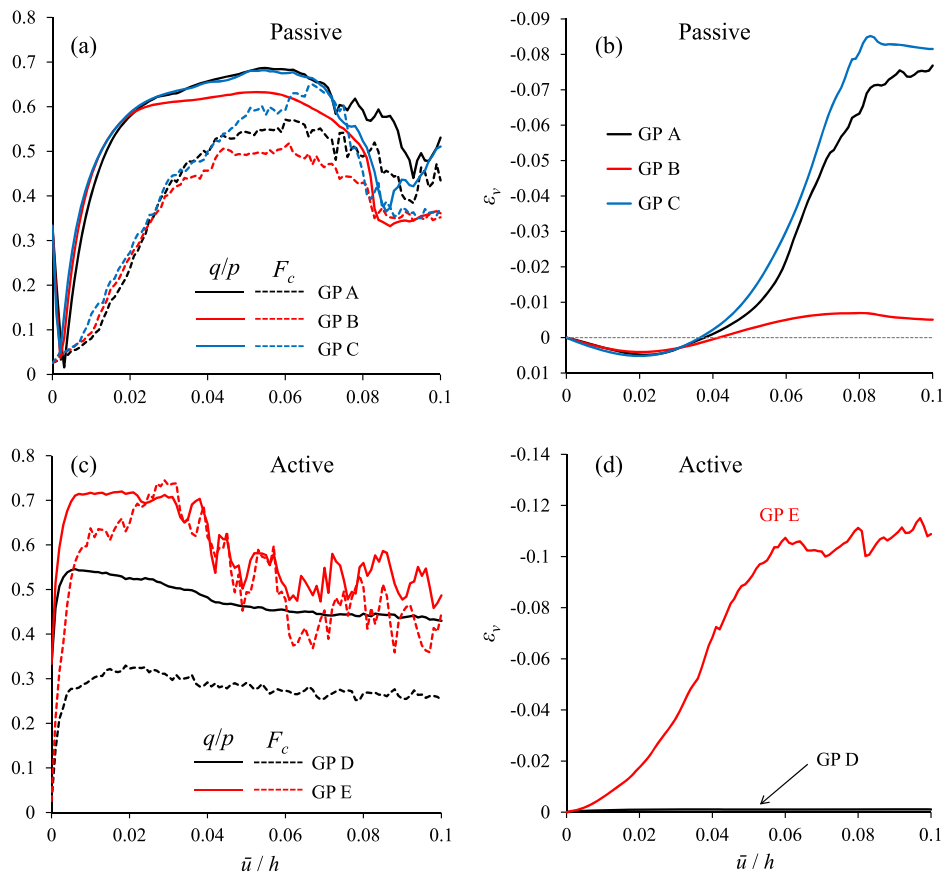


Figure 11. Selected Gauss point (see Figures 7(a) and 10(a) on their locations) responses for the cases of a rough wall under the translation mode: (a),(b) passive failure; (c),(d) active failure.

evolutions of the volumetric strain  $\varepsilon_v$  at the three Gauss points. These points all experience overall contraction at the early stage of wall movement ( $\bar{u}/h < 0.04$ ) but diverge apparently with further wall movement. For GP A, which is inside the primary shear zone, its deformation is markedly large, and its dilation  $\varepsilon_v$  finally reaches about  $-0.08$ . However, for GP B, which is located in a region with small deformation, its volumetric change is rather small (less than 0.01) and the peak  $F_c$  of this point are also the smallest among the three points. The response of GP C, which is located inside the secondary shear zone, is very similar to that of GP A. But the dilation of GP C is slightly larger than that of GP A. This is because GP A has a much larger confining pressure than GP C, which partly suppresses the dilation of GP A and results in a smaller peak  $F_c$  for GP A than for GP C. For the two Gauss points under the active failure condition, their evolution curves are reminiscent of those from a monotonic loading test. The major principal direction of stress remains at the vertical direction. The increase of both  $q/p$  and  $F_c$  for the two points under the active failure condition is much faster than that under the passive one, which explains the instant decrease of active lateral earth pressure observed in Figure 5(b). As GP D is located outside the shear-localised zone, its deformation level is rather small. The peak stress ratio and the peak  $F_c$  at this point are much smaller than those of GP E, which is inside the shear zone as shown in Figure 11(c). Figure 11(d) indicates the two points begin to dilate upon wall movement without any initial contraction as in the passive failure condition. While the dilation of GP D is negligible, the dilation at GP E is rather noticeable, reaching about  $-0.12$  at the final stage.

It is instructive to show the microstructures of these local Gauss points at the final stage ( $\bar{u}/h = 0.1$ ), which can be better visualised from the contact force chain network of the RVE packings, as shown in Figure 12. For the passive failure mode, the RVE packing of GP A (inside the primary shear zone) deforms severely. Several distinct strong force chains are observable, which penetrate through the RVE packing. An overall anti-clockwise rotation of the packing is also found, which is consistent with that shown in Figure 7(a). In contrast to GP A, the deformation at GP B (outside the localised zones) is rather small. The packing still retains a square shape similar to its initial configuration. The force chain network is relatively homogeneous compared with that at GP A. The packing of GP C (inside the secondary shear zone) also deforms significantly. However, its strong force chains are not that obvious as compared with GP A, suggesting the stress level (both  $p$  and  $q$ ) of GP C is much smaller than that of GP A, even though their stress ratio is close. The overall rotation of the packing at GP C is clockwise, which is again consistent with that observed in Figure 7(a). For all three points, the major principal direction of stress is roughly horizontal because the strong force chains align approximately horizontal. For the active failure case, the packing of GP D (outside the localised zone) undergoes a negligibly small deformation as can be observed from the overall very thin force chain width in the network (Figure 12(b) left). In contrast, the deformation of the packing at GP E (inside the localised region) is extremely large with several strong force chains clearly found. Its overall clockwise rotation is significant too. However, as compared with the passive failure cases, the force chains under the active failure condition are much thinner, indicating that the stress level at the active failure condition is much smaller. Again for both points, the major principal direction of stress is roughly vertical, as observed from the alignment of their strong force chains.

#### 4. FOOTING

The mesh and the boundary conditions for the multiscale modelling of the footing problem are shown in Figure 13 where the mesh is generated using the open-source software Gmsh [47]. Only half of the domain is modelled because of the symmetry of the problem, which is discretised into 2500 second-order triangular elements (each with six nodes and three Gauss points). A total of 7500 RVE packings containing 3 million particles need to be handled for every iteration in the simulation. It takes around 24 h of computation on an HP SL230 Gen8 server ( $2 \times 8$ -core 2.6 GHz CPU). The width of the modelled half-domain is 0.6 m and the depth 0.4 m. The half width of the footing is  $B/2 = 0.05$  m. The bottom of the domain is fixed in both directions, while the left and the right boundaries are only constrained by the horizontal displacement but are free to move in the vertical direction. The base of the footing can be either rough or smooth. The influence of this assumption

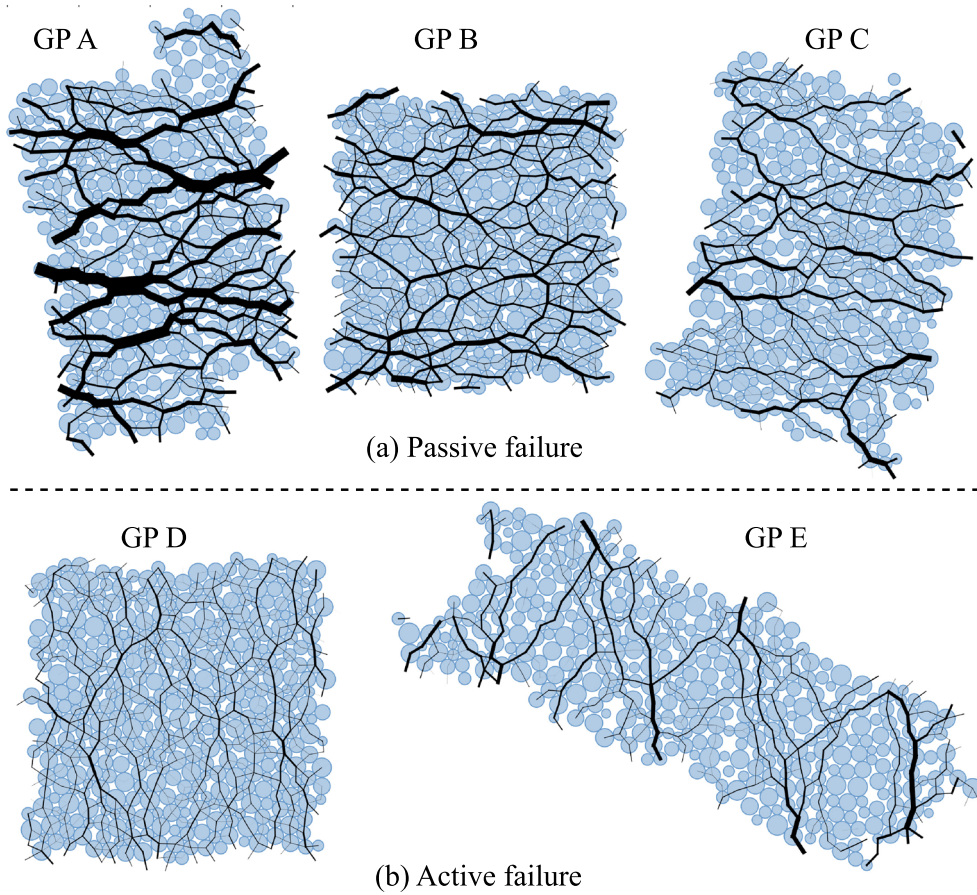


Figure 12. Force chain network of the selected local Gauss points (see Figures 7(a) and 10(a) on their locations) in the retaining wall problem at the final stage.

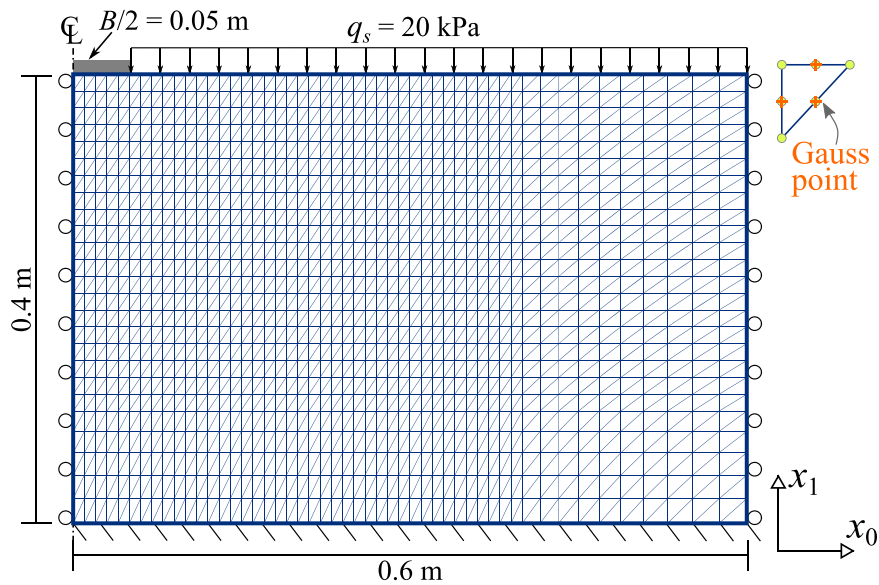


Figure 13. Mesh and boundary conditions for the footing problem.

is marginal as will be shown. A uniform vertical settlement  $d$  will be applied on the footing by assuming the footing is perfectly rigid. A surcharge of  $q_s = 20$  kPa is uniformly applied to the surface. Different from the retaining wall problem, all the RVE packings in the footing problem are isotropically consolidated to attain a mean effective stress of 20 kPa before settlement is applied to the footing. The initial void ratio for the uniform domain is  $e_0 = 0.187$ . Again gravity is neglected in the simulation.

#### 4.1. DEM model and RVE effective friction angle

DEM parameters chosen for the footing problem are summarised in Table II. Compared with the values used in the retaining wall problem, an increased Young's modulus of the particles  $E_c$  is adopted in this test to increase the macroscopic stiffness of the soil. We also decrease the interparticle friction angle  $\varphi$  and the rolling resistance coefficient  $\eta$  to obtain a more realistic effective friction angle  $\varphi'$  for fine sand. The changes to a larger stiffness (larger  $E_c$ ) but a smaller shear strength (smaller  $\varphi$  and  $\eta$ ) for the material make it easier to develop the general shear failure pattern in the footing problem.

Following the same procedure described in Section 3.1, we conducted drained biaxial compression tests on the RVE and drew two Mohr's circles. The effective friction angle for the RVE is estimated as  $\varphi' \approx 30.5^\circ$  from the envelope of the two circles as shown in Figure 14. The inset shows the stress–strain responses of the two drained biaxial compression tests. Note that compared with the effective friction angle in the retaining wall problem, the fitted value here is more realistic for a sandy soil [42].

#### 4.2. Bearing capacity

The evolution of the vertical stress  $\sigma_v$  exerted on the footing base (normalised by the surcharge  $q_s$ ) is plotted against the footing settlement  $d$  (normalised by the footing width  $B (= 0.1$  m)) in Figure 15 where the responses from using a rough footing are compared against those with a smooth

Table II. Parameters for the DEM model used in the footing problem.

$E_c$ (MPa)	$\nu_c$	$\beta_c$	$\varphi$ ( $^\circ$ )	$\eta$	$\alpha$
800	0.5	1.0	23	0.05	0.1

DEM, discrete element method.

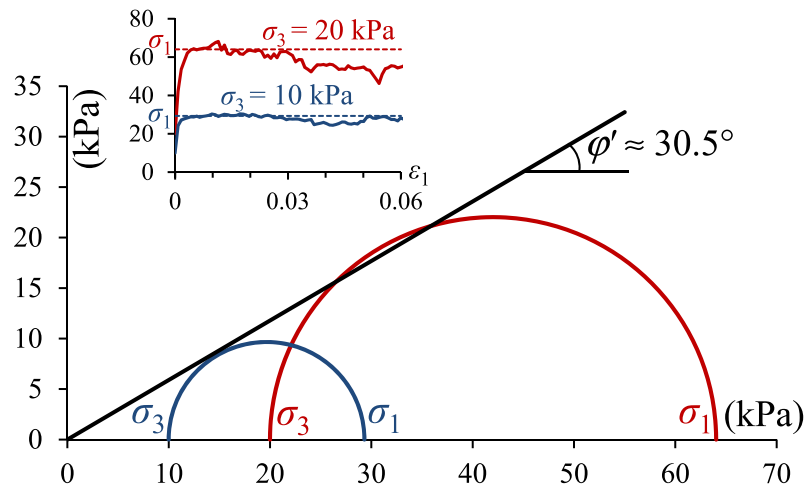


Figure 14. Estimation of the macroscopic friction angle of the representative volume element for the footing problem.

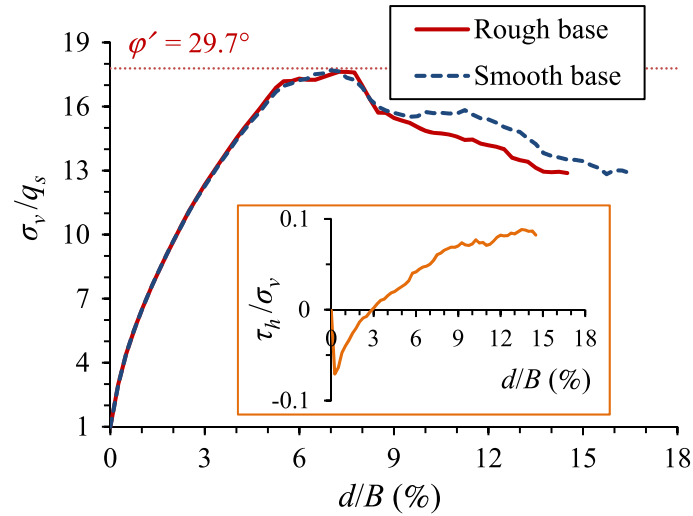


Figure 15. Evolution of the vertical stress normalised by the surcharge exerted on the footing. The inset shows the evolution of shear stress normalised by the vertical stress on the rough footing.

footing. Evidently, in both cases, their pre-peak behaviours are almost identical, and a softening behaviour is found after the peak stress state. There is certain difference in their post-peak responses, but it is rather small. From the inset of Figure 15, we can see the shear stress  $\tau_h$  on the rough footing during the settling process is an order smaller in magnitude than the normal vertical stress. Its influence on the bearing capacity of the footing is thus negligible. Progressive failure occurs at early stage of the settling ( $d/B < 3\%$ ), where punching shear failure dominates the deformation mode of the foundation soil. A triangular-wedge-shaped soil block beneath the footing emerges and tends a leftward movement, resulting in a negative shear stress on the footing base. After significant settlement, the deformation pattern tends to become the general shear failure type where a large bulk of soil under and surrounding the footing heaves rightwards, causing a positive shear stress on the footing base. The shear failure patterns can be seen in Figure 16 and will be discussed in the next subsection.

We further compare the simulation results with the following Prandtl’s solution [2] of the ultimate bearing capacity  $p_u$  for a shallow footing seated on a weightless, cohesionless soil:

$$p_u = q_s N_q, \tag{21}$$

where  $N_q$  is the bearing capacity coefficient due to surcharge, and can be determined from the effective friction angle

$$N_q = \tan^2 \left( \frac{\pi}{4} + \frac{\varphi'}{2} \right) e^{\pi \tan \varphi'} = K_p e^{\pi \tan \varphi'}. \tag{22}$$

As the current simulation results give  $N_q = 17.8$  indicated by Figure 15, it corresponds to an effective friction angle of  $\varphi' = 29.7^\circ$  based on Equation 22. This is indeed close to the fitted value of  $30.5^\circ$  for the RVE packing from Figure 14.

#### 4.3. Failure zone

Figure 16 depicts the final contours of the accumulated shear strain  $\varepsilon_q$ , the void ration  $e$ , the accumulated average particle rotation  $\bar{\theta}$  and the displacement vector field  $\mathbf{u}$  in the problem domain after a settlement of  $d = 14.5$  mm for the rough footing. Figure 16(a) manifests a general shear failure pattern in the foundation soil despite a much clearer punching triangular wedge than the log-spiral slip line in the general failure zone. The penetrating wedge beneath the footing base moves downwards as a rigid body in large. The angle of the wedge with respect to the horizontal surface is  $67^\circ$  as measured from Figure 16(a), which is different from the Terzaghi’s assumption that the wedge

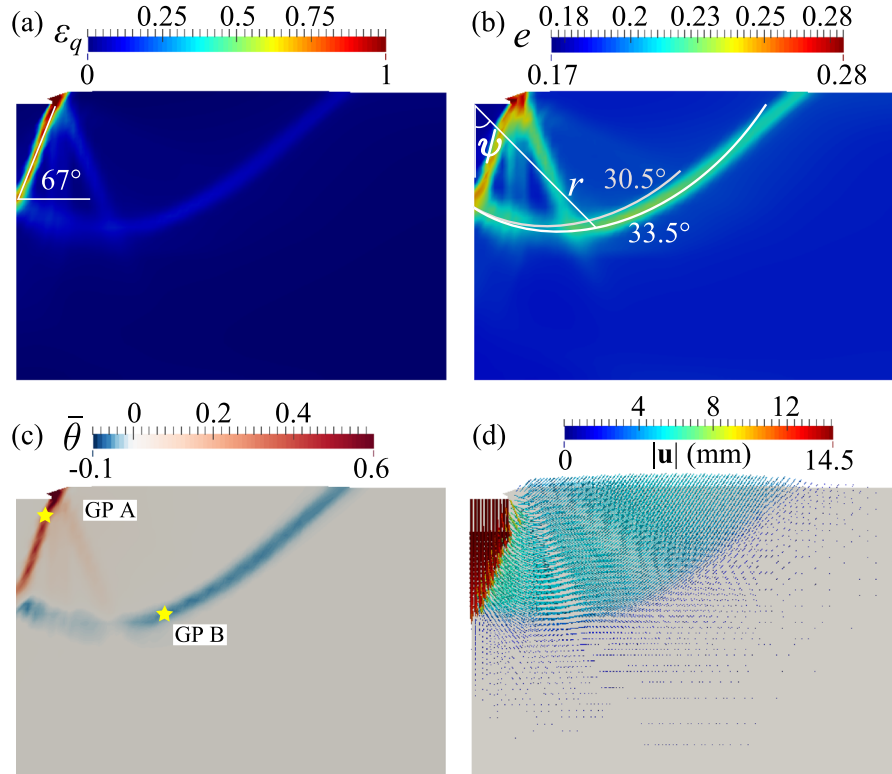


Figure 16. Contours of (a) accumulated shear strain, (b) void ratio, (c) accumulated average particle rotation and (d) displacement field for the footing problem.

angle is equal to the effective friction angle  $\varphi'$ . According to some experimental data, Vesić [48] concluded that the wedge corresponds to the Rankine's active failure zone and modified the angle to  $\pi/4 + \varphi'/2 \approx 60.25^\circ$ . The wedge angle from the simulation is also slightly larger than the value modified after Vesić but already close enough. One possible reason is that the current deformation pattern is more dominated by the punching shear failure beneath the footing, while the shear slip zones in the general failure mode are relatively weak.

The general shear failure pattern is more clearly seen from the void ratio contour as shown in Figure 16(b). From the figure, it is apparent that a third shear slip line emerges from the footing edge down-rightwards and is intercepted by the general failure slip line. The general shear failure slip line can be approximately described by a log-spiral curve as follows:

$$r = r_0 e^{\psi \tan \varphi'}, \quad (23)$$

where  $\psi$  measures the direction (with regard to the vertical axis) of the line connecting the centre of the footing and the point located on the log-spiral curve,  $r$  is the length of the line and  $r_0$  is the line length when  $\psi = 0^\circ$  and is also the height of the inverted triangular wedge. Two such curves with  $\varphi' = 30.5^\circ$  and  $33.5^\circ$ , respectively, are superimposed in Figure 16(b), which match the simulated general failure slip line reasonably well. The used values of the effective friction angle are close to the fitted one for the RVE packing in Figure 14.

The contour of the accumulated average particle rotation, shown in Figure 16(c), also clearly depicts the general shear failure pattern. Inside the punching shear zone, particles mainly rotate anti-clockwise (positive  $\bar{\theta}$ ), while those inside the general failure slip line rotate clockwise (negative  $\bar{\theta}$ ). However, as the shear strain in the general failure slip line is much weaker than that in the punching shear zone, the magnitude of the clockwise rotation is much smaller than that of the anti-clockwise rotation (note that the colour bar ranges from  $-0.1$  to  $0.6$ ). Furthermore, the punching of

the triangular wedge beneath the footing and the heaving of the bulk soil beside the footing can be clearly seen from the displacement vector plot in Figure 16(d).

#### 4.4. Local analyses

Similar to that in Section 3.4, we can further examine the local responses and the microstructures for some Gauss points of interest. Two Gauss points are selected whose positions are marked in Figure 16(c). GP A is located inside the shear zone of the punching wedge, and GP B is inside the general failure spiral line. Figure 17 presents the evolutions of the stress ratio  $q/p$ , the fabric anisotropy  $F_c$  and the volumetric strain  $\varepsilon_v$  of the two points against the footing settlement. While the stress ratio of both points shows an increase followed by a decrease trend, the increase of  $q/p$  at GP A is much faster than that at GP B. The difference is even more appreciable for the increase of fabric anisotropy. At GP A, the change of the local structure is instant as the footing begins to settle. The change of the local structure at GP B is rather slow in pace. Similar trend can be observed from the dilation curves of the two points. Following a small contraction, GP A begins to dilate significantly after  $d/B = 0.03$ , while for GP B, an obvious dilation is not observed until  $d/B > 0.08$ . The difference in evolution at the two Gauss points clearly corroborates the progressive failure nature of the footing problem, that is, the local punching failure dominates before the general failure is formed at a relatively large footing settlement.

The force chain network of the two Gauss points at the final stage ( $d/B = 0.145$ ) is shown in Figure 18. As can be seen, the deformation level at GP A is rather large. The RVE packing is severely distorted with a clearly overall anti-clockwise rotation. A few penetrating strong force

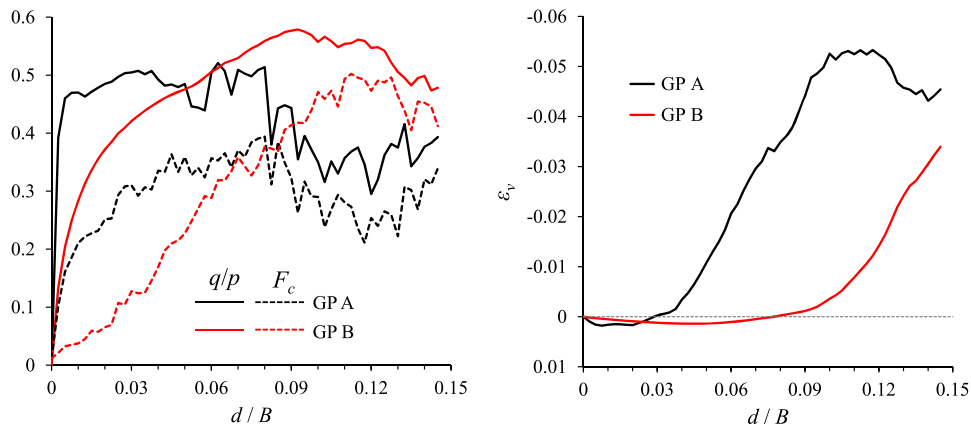


Figure 17. Selected Gauss point responses in the footing problem.

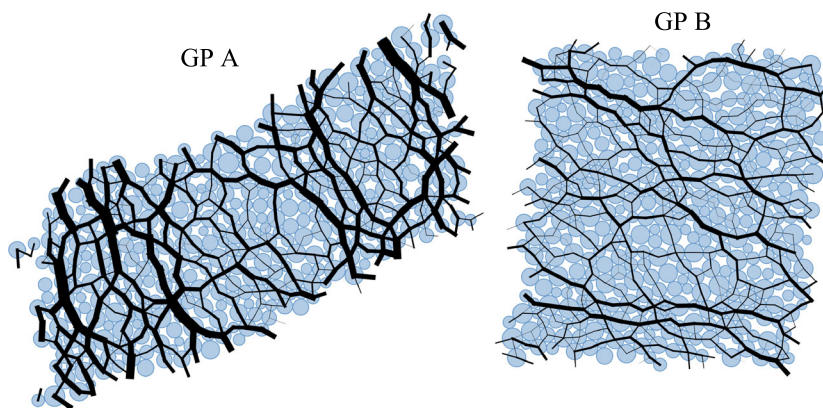


Figure 18. Force chain network of the selected local Gauss points in the footing problem at the final stage.

chains are found inside the packing. These are in great contrast with the relatively small deformation and less-distinct force chains in the GP B case. The packing at GP B as a whole undergoes a mild clockwise rotation. The opposite rotation directions for GP A and GP B are consistent with that observed in Figure 16(c). The difference in the alignments of the strong force chains inside the two RVE packings indicate the major principal stress directions at this two points are different from each other.

## 5. CONCLUDING REMARKS

The paper presented a novel computational multiscale modelling approach based on hierarchical coupling of FEM and DEM in application to two classical geotechnical problems – the retaining wall and the footing. This hierarchical multiscale modelling approach adopts FEM to solve the continuum-level BVPs and assigns DEM packings to the Gauss points of the FEM mesh to derive the local material responses from independent simulations. In doing so, the phenomenological nature inherent to conventional continuum modelling approaches can be avoided. It is demonstrated this multiscale approach is capable to predict the passive and the active lateral earth pressure coefficients, and the bearing capacity of shallow foundations, as well as very complicated failure patterns in these problems. The simulations compared reasonably well with available analytical solutions (which have been derived based on certain assumptions). It is not surprising because the framework, with its embedded DEM simulation at the mesoscale/microscale, could naturally incorporate the material nonlinearity and plasticity originated from the particle level in the continuum-scale computation. Further, cross-scale analyses and correlation of observations on the macroscopic failure patterns and the strong force chain network and particle rotations confirm the validity, robustness and predictive capability of the proposed method. Some main findings from the study are summarised in the following.

1. To obtain the realistic macroscopic friction angle for a real sand/gravel, rolling resistance needs to be considered in the DEM model if simplified circular/spherical particles are used to compensate for the particle shape effect. The effective friction angle of the material is then determined from the element tests on the RVE packing based on Mohr's circles. The microscopic parameters in the DEM model, which are the only parameters required in the current hierarchical multiscale approach, can be calibrated from laboratory tests on sand/gravel.
2. The numerically determined passive and active lateral earth pressure coefficients are close to the theoretical predictions by Rankine. The assumption of a rough or a smooth wall under the translation mode yields very different  $K_p$  but similar  $K_a$ . While the translation mode gives the largest  $K_p$  but the smallest  $K_a$ , the rotation-about-top mode gives the smallest  $K_p$  and the largest  $K_a$ . The lateral earth pressure coefficients under both the passive and the active failure conditions for the rotation-about-bottom mode lie in between the other two modes. Furthermore, the active earth pressure decreases more quickly than the increase of the passive earth pressure, which can be explained from the local analyses of some selected Gauss points. The mobilisation of the microstructural response of the RVE packings is much slower in the passive failure than in the active failure.
3. The shear-zone pattern for the passive failure under the translation mode with a rough wall shows two major shear bands. The primary one emerges from the heel of the wall and propagates towards the surface of the backfill soil. The secondary one emanates from the top of the wall and pierces into the soil and is intercepted by the primary one. For the corresponding smooth wall case, there exists only one shear band depicting a look of straight line and an angle with regard to the horizontal surface very close to the Rankine's theoretical value for passive failure. The shear band for the active condition under translation mode with either a rough or a smooth wall shows a single straight line pattern with an angle with regard to the horizontal surface close to the Rankine's theoretical value for active failure. The simulation results show good agreements with both experimental observations and FEM predictions [15, 16, 40].
4. The simulated ultimate bearing capacity of the shallow footing matches the Prandtl's solution fairly well. A general shear failure pattern is observed, where the failure zone consists of a

punching triangular wedge right beneath the footing and a shear slip line tending towards the ground surface of the soil. The angle of the wedge with respect to the horizontal surface is slightly larger than the Vesic's modification [48], that is, the angle of the Rankine's active failure line. The general failure slip line can be largely described by a log-spiral curve. The local analyses of the two Gauss points (one inside the wedge shear zone, the other inside the slip line) indicate a progressive failure mode for the footing problem.

5. Besides the shear strain and the void ratio contours that are commonly used, the contour of accumulated average particle rotation proves to be an additional good indicator for the analysis of strain localisation. While severe particle rotations generally take place inside the shear bands, the directions of particle rotations within different shear zones could be opposite, such as the cases of the passive failure under translation mode for the rough retaining wall and the general shear failure for the footing.

The focus of the study has been placed on demonstrating the applicability of the hierarchical multiscale approach in solving practical geotechnical problems. Related to the study, there are several exploratory topics meriting continuous investigations. For example, considering the heterogeneity of geomaterials in a natural setting, it appears more reasonable if the properties of geomaterials are considered to be spatially random [49, 50]. By assigning different RVE packings (e.g. varying initial void ratios) to the Gauss points, the influence of inherent heterogeneity of natural sand can be studied using this approach. Besides the static problems already treated here, dynamic loading is of major interest to earthquake engineers and can be studied based on this approach with moderate modifications as well, for example by considering viscosity in the DEM model and inertia terms in the FEM solution. In addition, the micro–macro bridging capability of the proposed approach needs to be further explored to assist a comprehensive understanding of the physics and mechanics governing the shear behaviour of granular soils. The topics listed earlier are important continuations of the study, which are practically tractable. Meanwhile, there are more formidable challenges pertaining to the multiscale approach, which may need a coordinated effort among different parties, for example numerical modellers, experimentalists, computer scientists and physicists. The following provides a number of examples.

1. The hierarchical multiscale approach relies crucially on the DEM part to provide reliable, quantitative predictions, while it remains challenging to accurately calibrate the DEM model parameters. Indeed, if the rolling resistance model or the clumped particle model is used in the DEM, a common way of calibration remains to be curve fitting, which is essentially phenomenological. To overcome this obstacle, proper characterisation and modelling of the particle shape need to be implemented in DEM. Some recent progresses have been made in this regard, for example [51–53]. However, how to effectively implement the generated complex-shaped particles into DEM remains a bottleneck, which may need the help from computer scientists and applied mathematicians. Meanwhile, advanced particle-scale tests [54, 55] are required to provide essential microscopic parameters such as the contact moduli and the inter-particle friction angle for the DEM simulation. This will constitute a key step towards real application of the multiscale approach to geotechnical designs.
2. Inherited from the adopted conventional continuum model, the solution of the current hierarchical multiscale approach is found dependent on element type [24] though being less sensitive to mesh density. It is because in upscaling the Gauss point responses to the FEM, the information of the intrinsic length of the material is lost. For a problem with material softening, the BVP could be ill-posed. To tackle this issue, a simple nonlocal regularisation [56] could be employed, which is currently examined by the authors.
3. The success of the multiscale approach depends critically on its computational efficiency. On one hand, we may seek more computing power by virtue of the parallel structure of the framework; on the other hand, the computational algorithm of the approach needs to be pushed to a new level of efficiency too. For example, further effort needs to be made to find a consistent tangent operator, which can provide quadratic convergence for the Newton–Raphson iteration.
4. How to consider the presence of pore fluid in sand in the multiscale approach is another challenge. A full consideration of the influence of pore fluid may require a further coupling of the

DEM with another software simulating the behaviour of pore fluid, such as lattice Boltzmann method or computational fluid dynamics method, for each RVE, which inevitably poses great challenges to the hierarchical formulation, specification of macro/micro boundary condition and handling of the computational cost that increases by orders of magnitude.

## ACKNOWLEDGEMENTS

We thank the two anonymous reviewers for their constructive comments. The second author also wishes to thank Prof. Itai Einav for suggesting the multiscale study of the footing problem during a conversation in the IWBDG 2014 conference. We acknowledge the support from Science School Computational Science Initiative, HKUST, for allowing us to access its HPC facility. The study was financially supported by Research Grants Council of Hong Kong (GRF Grant No. 623211).

## REFERENCES

1. Rankine WJM. On the stability of loose earth. *Philosophical Transactions of the Royal Society of London* 1857; **147**:9–27.
2. Prandtl L. Über die Härte plastischer Körper. *Nachrichten von der Königlichen Gesellschaft der Wissenschaften, Göttingen, Math.-Phys. Klasse* 1920; **1920**:74–85.
3. Terzaghi K. *Theoretical Soil Mechanics*. Wiley: New York, 1943.
4. Taylor DW. *Fundamentals of Soil Mechanics*. Wiley: New York, 1948.
5. Drucker DC, Prager W, Greenberg HJ. Extended limit design theorems for continuous media. *Quarterly of Applied Mathematics* 1952; **9**:381–389.
6. Prager W. The general theory of limit design. *Proceedings of the 8th International Congress of Theoretical and Applied Mechanics (Istanbul 1952)*, Istanbul, 1955; 65–72.
7. Gutierrez M, Ishihara K. Non-coaxiality and energy dissipation in granular material. *Soils and Foundations* 2000; **40**:49–59.
8. Yu HS, Yuan X. On a class of non-coaxial plasticity models for granular soils. *Proceedings of the Royal Society A* 2006; **462**(2067):725–748.
9. Casagrande A, Carillo N. Shear failure of anisotropic materials. *Proceedings of Boston Society of Civil Engineers* 1944; **31**:74–87.
10. Arthur JRF, Menzies BK. Inherent anisotropy in a sand. *Géotechnique* 1972; **22**(1):115–128.
11. Arthur JRF, Chua KS, Dunstan T. Induced anisotropy in a sand. *Géotechnique* 1977; **27**(1):13–30.
12. Roscoe KH, Schofield AN, Wroth CP. On the yielding of soils. *Géotechnique* 1958; **8**(1):22–53.
13. Schofield AN, Wroth CP. *Critical State Soil Mechanics*. McGraw-Hill: London, UK, 1968.
14. Vardoulakis I. Deformation of water-saturated sand: I. Uniform undrained deformation and shear band. *Géotechnique* 1996; **46**(3):441–456.
15. Nübel K, Huang W. A study of localized deformation pattern in granular media. *Computer Methods in Applied Mechanics and Engineering* 2004; **193**(27–29):2719–2743.
16. Teichman J. FE-analysis of patterning of shear zones in granular bodies for earth pressure problems of a retaining wall. *Archives of Hydro-Engineering and Environmental Mechanics* 2004; **51**(4):317–348.
17. Desrues J, Viggiani G. Strain localization in sand: an overview of the experimental results obtained in Grenoble using stereophotogrammetry. *International Journal for Numerical and Analytical Methods in Geomechanics* 2004; **28**(4):279–321.
18. Banimahd M, Woodward PK. Load-displacement and bearing capacity of foundations on granular soils using a multi-surface kinematic constitutive soil model. *International Journal for Numerical and Analytical Methods in Geomechanics* 2006; **30**:865–886.
19. Gao Z, Zhao J. Strain localization and fabric evolution in sand. *International Journal of Solids and Structures* 2013; **50**:3634–3648.
20. Conte E, Donato A, Troncone A. Progressive failure analysis of shallow foundations on soils with strain-softening behaviour. *Computers and Geotechnics* 2013; **54**:117–124.
21. Terzaghi K. Old earth pressure theories and new test results. *Engineering News Record* 1920; **85**:632–637.
22. Cundall PA, Strack ODL. A discrete numerical model for granular assemblies. *Géotechnique* 1979; **29**(1):47–65.
23. Guo N, Zhao J. A hierarchical model for cross-scale simulation of granular media. In *AIP Conference Proceedings*, Vol. 1542, Yu A (ed.). AIP Publishing: Sydney, Australia, 2013; 1222–1225.
24. Guo N, Zhao J. A coupled FEM/DEM approach for hierarchical multiscale modelling of granular media. *International Journal for Numerical Methods in Engineering* 2014; **99**(11):789–818.
25. Guo N. Multiscale characterization of the shear behavior of granular media. *Ph.D. Thesis*, Hong Kong, 2014.
26. Zhao J, Guo N. The interplay between anisotropy and strain localisation in granular soils: a multiscale insight. *Géotechnique* 2015. DOI: 10.1680/geot.14.P.184.
27. Meier HA. Computational homogenization of confined granular media. *Ph.D. Thesis*, 2009.
28. Miehe C, Dettmar J, Zäh D. Homogenization and two-scale simulations of granular materials for different microstructural constraints. *International Journal for Numerical Methods in Engineering* 2010; **83**:1206–1236.

29. Andrade J, Avila C, Hall S, Lenoir N, Viggiani G. Multiscale modeling and characterization of granular matter: from grain kinematics to continuum mechanics. *Journal of the Mechanics and Physics of Solids* 2011; **59**:237–250.
30. Nitka M, Combe G, Dascalu C, Desrues J. Two-scale modeling of granular materials: a DEM-FEM approach. *Granular Matter* 2011; **13**(3):277–281.
31. Nguyen TK, Combe G, Caillerie D, Desrues J. FEM  $\times$  DEM modelling of cohesive granular materials: numerical homogenisation and multi-scale simulations. *Acta Geophysica* 2014; **62**(5):1109–1126.
32. Oda M, Konishi J, Nemat-Nasser S. Experimental micromechanical evaluation of strength of granular materials: effects of particle rolling. *Mechanics of Materials* 1982; **1**:269–283.
33. Ishihara K, Oda M. Rolling resistance at contacts in simulation of shear band development by DEM. *Journal of Engineering Mechanics* 1998; **124**(3):285–292.
34. Zhao J, Guo N. Rotational resistance and shear-induced anisotropy in granular media. *Acta Mechanica Solida Sinica* 2014; **27**(1):1–14.
35. Šmilauer V, Catalano E, Chareyre B, Dorofeenko S, Duriez J, Gladky A, Kozicki J, Modenese C, Scholtès L, Sibille L, Stránský J, Thoeni K, *et al.* Yade reference documentation. In *Yade Documentation*, (1st edn), Šmilauer V. (ed.). The Yade Project, 2010.
36. Wren JR, Borja RI. Micromechanics of granular media Part II: overall tangential moduli and localization model for periodic assemblies of circular disks. *Computer Methods in Applied Mechanics and Engineering* 1997; **141**:221–246.
37. Krut N, Rothenburg L. Statistical theories for the elastic moduli of two-dimensional assemblies of granular materials. *International Journal of Engineering Science* 1998; **36**:1127–1142.
38. Luding S. Micro-macro transition for anisotropic, frictional granular packings. *International Journal of Solids and Structures* 2004; **41**:5821–5836.
39. Wensrich CM. Stress, stress-asymmetry and contact moments in granular matter. *Granular Matter* 2014; **16**:597–608.
40. Widuliński Ł., Tejchman J, Kozicki J, Leśniewska D. Discrete simulations of shear zone patterning in sand in earth pressure problems of a retaining wall. *International Journal of Solids and Structures* 2011; **48**:1191–1209.
41. Kozicki J, Tejchman J, Mühlhaus HB. Discrete simulations of a triaxial compression test for sand by DEM. *International Journal for Numerical and Analytical Methods in Geomechanics* 2014; **38**:1923–1952.
42. Meyerhof GG. Penetration tests and bearing capacity of cohesionless soils. *Journal of the Soil Mechanics and Foundations Division* 1956; **82**(1):1–19.
43. Hall SA, Bornert M, Desrues J, Pannier Y, Lenoir N, Viggiani G, Bésuelle P. Discrete and continuum analysis of localised deformation in sand using X-ray  $\mu$ CT and volumetric digital image correlation. *Géotechnique* 2010; **60**(5):315–322.
44. Bardet JP, Proubet J. A numerical investigation of the structure of persistent shear bands in granular media. *Géotechnique* 1991; **41**(4):599–613.
45. Satake M. Fabric tensor in granular materials. In *IUTAM Symposium on Deformation and Failure of Granular Materials*. A.A. Balkema: Delft, 1982; 63–68.
46. Oda M. Fabric tensor for discontinuous geological materials. *Soils and Foundations* 1982; **22**(4):96–108.
47. Geuzaine C, Remacle JF. Gmsh: a 3-D finite element mesh generator with built-in pre- and post-processing facilities. *International Journal for Numerical Methods in Engineering* 2009; **79**:1309–1331.
48. Vesić AS. Analysis of ultimate loads of shallow foundations. *Journal of the Soil Mechanics and Foundations Division* 1973; **99**(1):45–73.
49. Andrade JE, Baker JW, Ellison KC. Random porosity fields and their influence on the stability of granular media. *International Journal for Numerical and Analytical Methods in Geomechanics* 2008; **32**:1147–1172.
50. Chen Q, Seifried A, Andrade JE, Baker JW. Characterization of random fields and their impact on the mechanics of geosystems at multiple scales. *International Journal for Numerical and Analytical Methods in Geomechanics* 2012; **36**:140–165.
51. Mollon G, Zhao J. Fourier-Voronoi-based generation of realistic samples for discrete modelling of granular materials. *Granular Matter* 2012; **14**:621–638.
52. Mollon G, Zhao J. Generating realistic 3D sand particles using Fourier descriptors. *Granular Matter* 2013; **15**:95–108.
53. Mollon G, Zhao J. 3D generation of realistic granular samples based on random fields theory and Fourier shape descriptors. *Computer Methods in Applied Mechanics and Engineering* 2014; **279**:46–65.
54. Hall SA, Wright J, Pirling T, Andò E, Hughes DJ, Viggiani G. Can interparticle force transmission be identified in sand? First results of spatially-resolved neutron and X-ray diffraction. *Granular Matter* 2011; **13**:251–254.
55. Senetakis K, Coop MR, Todisco MC. The inter-particle coefficient of friction at the contacts of Leighton Buzzard sand quartz minerals. *Soils and Foundations* 2013; **53**:746–755.
56. Bažant Z, Jirásek M. Nonlocal integral formulations of plasticity and damage: survey of progress. *Journal of Engineering Mechanics* 2002; **128**:1119–1149.